Novel Undamped Gapless Plasmon Mode in a Tilted Type-II Dirac Semimetal

Krishanu Sadhukhan,[1] Antonio Politano,[2,3] and Amit Agarwal[1,*]
[1]*Department of Physics, Indian Institute of Technology, Kanpur 208016, India*
[2]*Dipartimento di Scienze Fisiche e Chimiche (DSFC), Università dell'Aquila, Via Vetoio 10, I-67100 L'Aquila, Italy*
[3]*CNR-IMM Istituto per la Microelettronica e Microsistemi, VIII strada 5, I-95121 Catania, Italy*

(Received 24 April 2019; published 31 January 2020)

We predict the existence of a novel long-lived gapless plasmon mode in a type-II Dirac semimetal (DSM). This gapless mode arises from the out-of-phase oscillations of the density fluctuations in the electron and the hole pockets of a type-II DSM. It originates beyond a critical wave vector along the direction of the tilt axis, owing to the momentum separation of the electron and hole pockets. A similar out-of-phase plasmon mode arises in other multicomponent charged fluids as well, but generally, it is Landau damped and lies within the particle-hole continuum. In the case of a type-II DSM, the open Fermi surface prohibits low-energy finite momentum single-particle excitations, creating a "gap" in the particle-hole continuum. The gapless plasmon mode lies within this particle-hole continuum gap and, thus, it is protected from Landau damping.

DOI: 10.1103/PhysRevLett.124.046803

The topological semimetal state in crystalline solids allows for the existence of relativistic quasiparticles, which have no analog in the Standard Model [1,2]. Protected by crystalline symmetries, tilted type-I and type-II Dirac (DSM) and Weyl semimetal (WSM) phases [3] are examples of this class of materials [4–7]. For a tilted DSM, the electronic dispersion is a sum of "potential" and "kinetic" terms, $E_{\mathbf{k}} = U_{\mathbf{k}} \pm T_{\mathbf{k}}$, where both the terms vanish at the fourfold degenerate (including spin) Dirac point [8,9]. The first term is odd along a specific direction of $\mathbf{k}$ (the "tilt" direction), while the second term has the usual form of an anisotropic massless Dirac cone. The DSM phase is type-II if the Dirac cone is tilted over, or $U_{\mathbf{k}} > T_{\mathbf{k}}$ along the tilt direction, otherwise it is classified as type-I DSM. Experimental realizations of a type-I DSM include Na_3Bi [10,11] and Cd_3As_2 [12,13] among others. Type-II DSM phase has been identified in $PtTe_2$ [8,9,14], $PtSe_2$ [15], and $PdTe_2$ [14,16,17], among others.

The Fermi surface in a type-I DSM is an ellipsoid enclosing a single type of carrier pocket (either electron or hole), with a vanishing density of states at the Dirac point. Contrarily, the Fermi surface of a type-II DSM is a hyperboloid with *open* electron and hole pockets along the tilt axis, as shown in Figs. 1(a)–1(d). The presence of both types of carriers at the Fermi energy in a type-II DSM leads to several interesting magnetotransport and optical properties [18,19]. Here, we explore collective density excitations in a type-II DSM [9,20] and predict the existence of a novel undamped gapless plasmon mode.

The presence of both electron and hole pockets at the Fermi energy in a type-II DSM suggests the possibility of two plasmon modes, related to the in-phase and the out-of-phase oscillation of the density deviations in the two electron fluids. The in-phase oscillation leads to the normal gapped plasmon mode in three-dimensional systems [21], while the out-of-phase oscillations generally lead to gapless plasmon mode. A similar gapless plasmon mode has been reported in other two-component systems, including spatially separated electron liquids [22,23], bilayer graphene [23], and spin-polarized systems [24]. However, the out-of-phase gapless mode is generally damped, as it lies within the particle-hole continuum (PHC) [22,23,23,24]. In contrast to this, we show that in type-II DSM the out-of-phase plasmon mode is undamped.

Our demonstration of this novel gapless plasmon mode in type-II DSM is based on hydrodynamic theory, along with exact analytical calculation of the density response function. The gapless plasmon mode appears beyond a critical wave vector on account of the momentum separation of electron and hole pockets along the tilt axis. The hyperboloidal open Fermi surface in a type-II DSM prohibits particle-hole excitations for vanishing energies and finite wave vectors along the tilt axis, creating a "PHC gap" in the single-particle excitation spectrum. The predicted gapless plasmon mode lies within this PHC gap, protected from Landau damping, and is *long-lived* for small energies.

The oppositely tilted Dirac nodes generally appear in pairs on different k points [4] located on the high-symmetry rotation axis (chosen to be the $\hat{z}$ axis). For simplicity, we consider DSM hosting one pair of Dirac nodes tilted along the $\hat{z}$ axis, as in several materials [8–13,15–17,25]. A simple low-energy Hamiltonian for each Dirac node has a block diagonal form with two 2×2 matrices [26], $\mathcal{H}_\chi$ and $\mathcal{H}_\chi^*$, where

$$\mathcal{H}_\chi = \hbar v_F[\chi\beta k_z\sigma_0 + k_x\sigma_x + k_y\sigma_y + k_z\sigma_z]. \quad (1)$$

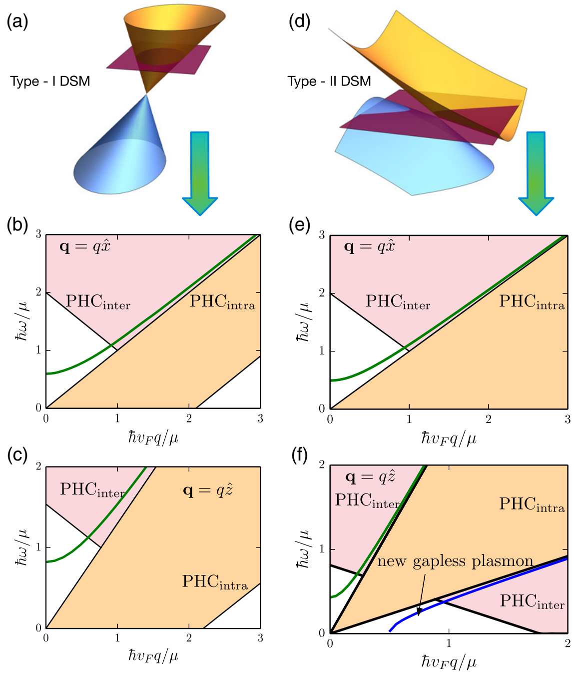

FIG. 1. Schematic of the band structure ($\varepsilon_{\mathbf{k}}$) of DSM node for a (a) type-I and (d) type-II DSM. The closed elliptic Fermi surface with an electron pocket in a type-I DSM and the open hyperbolic Fermi surface with an electron and a hole pocket in type-II DSM is evident. (b),(c) The PHC along with the gapped plasmon mode for a type-I DSM for q along the $\hat{x}$ and $\hat{z}$ direction. (e),(f) The PHC and the plasmon modes of type-II DSM along the $\hat{x}$ and $\hat{z}$ direction. The low-energy particle-hole gap and the novel gapless plasmon mode (blue line) are also shown. Here, $v_F = 0.65 \times 10^6$ m/s, and $\beta = 0.3(1.4)$ for a type-I (type-II) DSM.

Here, v_F denotes the isotropic Fermi velocity, $\chi = \pm 1$ is the node index, σ_i are the Pauli spin matrices, and σ_0 is the (2×2) unit matrix. The case of anisotropic Fermi velocities is discussed in the Supplemental Material [27]. Depending on the tilt parameter β, the boundaries of the Dirac cone along the z axis have either the opposite or same sign of their slopes, resulting in a type-I ($\beta < 1$) or a type-II DSM ($\beta > 1$). The energy dispersion for a given Dirac node is given by

$$\varepsilon^{\chi}_{\lambda\mathbf{k}} = \hbar v_F(\chi\beta k_z + \lambda k), \tag{2}$$

with $\lambda \pm 1$ being the band index denoting the conduction or valance band. The energy dispersion for both type-I and type-II DSM is shown in Figs. 1(a) and 1(d), respectively. The differing topology of the Fermi surfaces along the tilt axis is evident. While the Fermi surface for each node of a type-I DSM is a closed ellipsoid, type-II DSM has a pair of open hyperboloid Fermi surfaces along the tilt axis.

For an electron-doped type-I DSM with a closed Fermi surface, the structure of the PHC is very similar to that in an isotropic DSM [28,29]. The low-energy intraband single-particle transitions occur only for a continuous range of q values lying within the closed Fermi surface [see Figs. 1(b) and 1(c)]. Qualitatively, this also occurs in a type-II DSM for $\mathbf{q}$ perpendicular to the tilt axis (in the $\hat{x}$–$\hat{y}$ plane), as shown in Fig. 1(e).

Along the tilt axis ($\mathbf{q} = q\hat{z}$) in a type-II DSM, the open (hyperboloid) Fermi surface restricts all low-energy finite-q intraband transitions, causing the PHC to lie between the lines $\hbar\omega = v_F(\beta \pm 1)q$. More interestingly, the coexistence of an electron and a hole pocket in a type-II DSM results in low-energy interband transition for $q \geq q_{eh}$. Here,

$$q_{eh} = 2\mu/[\hbar v_F(\beta^2 - 1)] \tag{3}$$

quantifies the momentum separation between the electron and hole pockets for a fixed μ. This produces a PHC spectrum, which has a PHC gap in the low-energy finite-q regime for $q < q_{eh}$ [see Fig. 1(f)]. (See Secs. S2 and S3 of the Supplemental Material [27] for more details.) Below, we show that this PHC gap hosts a novel gapless Dirac plasmon mode.

To unveil the nature of the collective modes, we start with the hydrodynamics approach [30]. To this end, we first generalize the hydrodynamics approach to include (i) the anisotropic effective mass in DSM and (ii) the presence of two interacting charged fluids. In a type-I DSM, two electron liquids reside in different Dirac nodes with opposite tilt, giving them different mass. In a type-II DSM, the electron and hole liquids having different effective mass coexist in a single node itself. In the continuum limit, the electronic density fluctuation of the two fluids can be expressed as $n_a(\mathbf{r}, t) = n_{a0} + n_{a1}(\mathbf{r}, t)$, where $a = \{1, 2\}$. The corresponding electronic current density satisfies the local continuity equation: $\partial_t n_a + \nabla \cdot \mathbf{j}_a = 0$.

For these fluids interacting via Coulomb interactions, the Euler-Lagrange equation of motion is given by coupled vector equations for $a = \{1, 2\}$,

$$\mathcal{M}_a \frac{\partial \mathbf{j}_a}{\partial t} = -n_{a0}\nabla_{\mathbf{r}} \int d\mathbf{r}' \frac{e^2}{|\mathbf{r} - \mathbf{r}'|}[n_{11}(\mathbf{r}', t) + n_{21}(\mathbf{r}', t)]. \tag{4}$$

Here, $\mathcal{M}_a$ is the effective mass tensor of fluid a, and it multiplies the column vector of $\mathbf{j}_a$. For simplicity, we assume $\mathcal{M}_a$ to be diagonal matrix with the diagonal elements being m_{ai} for $i = \{x, y, z\}$. Using the continuity equation to eliminate $\mathbf{j}_a$ in Eq. (4), and by means of a Fourier transform, we obtain the equation for the long-wavelength dispersion of the collective modes to be

$$\mathrm{Det}\begin{pmatrix} \omega^2 - n_{10}V_q^{11}\sum_i \frac{q_i^2}{m_{1i}} & -n_{10}V_q^{12}\sum_i \frac{q_i^2}{m_{1i}} \\ -n_{20}V_q^{21}\sum_i \frac{q_i^2}{m_{2i}} & \omega^2 - n_{20}V_q^{22}\sum_i \frac{q_i^2}{m_{2i}} \end{pmatrix} = 0. \tag{5}$$

Here, V_q^{ab} is the Fourier transform of the Coulomb interactions between fluids a and b. For electron fluids interacting via unscreened Coulomb interaction, $V_q^{11} = V_q^{22} = V_q \equiv e^2/(\epsilon_0\epsilon_r q^2)$. In a type-II DSM, the electron and the hole pockets are separated in the momentum space (by q_{eh}), and hence, $V_q^{12} = V_q^{21} = V_{|q+q_{eh}|}$.

To incorporate the anisotropic effective mass in DSM, we use the following definition: $m_i^\lambda = \hbar^2 k_i/(\partial_{k_i}\varepsilon_{\lambda\mathbf{k}})$, with $\varepsilon_{\lambda\mathbf{k}}$ denoting the electronic dispersion. This reproduces the conventional effective mass for parabolic band systems, as well as the cyclotron mass in graphene: $m = \mu/v_F^2$. For the dispersion of Eq. (2) with $\mu > 0$, we obtain

$$m_{\{x,y,z\}}^{\lambda\chi} = \frac{\mu}{v_F^2}\frac{\lambda}{|\lambda + \chi\beta\cos\theta_q|}\left\{1, 1, \frac{\cos\theta_q}{(\chi\beta + \lambda\cos\theta_q)}\right\}. \quad (6)$$

Here, $\cos\theta_q = q_z/q$ is the polar angle of $\mathbf{q}$ [27]. In a type-II DSM, even for a given node with $\mu > 0$, we have $\lambda = \pm 1$, resulting in different effective masses for the electron and the hole pockets.

A type-I DSM node hosts a single charged fluid for any μ (electron liquid for $\mu > 0$), with an anisotropic mass. Thus, we find the conventional 3D gapped Dirac plasmons with anisotropic dispersion and different plasmon gap depending on the direction of approach to the $q \to 0$ limit,

$$\omega_{\rm pl}^2 \approx \frac{2n_e e^2 v_F^2}{\epsilon_0\epsilon_r\mu} \times \begin{cases} (1+\beta^2) + \mathcal{O}(q^2) & \text{for } \mathbf{q} = q\hat{z}, \\ 1 + \mathcal{O}(q^2) & \text{for } \mathbf{q} = q\hat{n}_{x-y} \end{cases}. \quad (7)$$

Here, $n_e = 2\mu^3/[3\pi^2\hbar^3 v_F^3(1-\beta^2)^2]$ is the total electron density (per Dirac node for $\mu > 0$, including spin) in a type-I DSM. Equation (7) reproduces the known result for the isotropic case without any tilt [29]. The plasmon dispersion for a type-I DSM, along with the corresponding PHC, is shown in Figs. 1(b) and 1(c).

The case of a type-II DSM hosting an electron and a hole pocket along the k_z axis is more interesting. Using Eq. (6) in Eq. (5), the plasmon dispersion along $\mathbf{q} = q\hat{z}$ is given by the roots of

$$\omega^2 = \frac{n_2 v_F^2 q^2}{\mu}[V_q(\beta+1)^2 - V_{|q+q_{eh}|}(\beta-1)^2]. \quad (8)$$

Here, $n_2 \approx \mu\mathcal{E}_{\rm max}^2/(12\pi^2\beta\hbar^3 v_F^3)$ denotes the cutoff ($\mathcal{E}_{\rm max}$) dependent electron (and hole) density for each node (with spin) of a type-II DSM. Equation (8) permits two solutions. One of these is the conventional gapped plasmon mode in the limit $q_z \to 0$, whose dispersion is given by

$$\omega_{\rm pl}^2 \approx \frac{n_2 e^2}{\epsilon_0\epsilon_r\mu} v_F^2(1+\beta)^2 + \mathcal{O}(q^2), \quad \text{for } \mathbf{q} = q\hat{z}. \quad (9)$$

In the x–y plane, the plasmon gap for a type-II DSM is identical to that of type-I DSM in Eq. (7), with the replacement $n_1 \to n_2$.

Interestingly, Eq. (8) permits another gapless solution (for $\omega \to 0$) beyond a critical wave vector, $q > q_c \equiv \mu\beta/[2\hbar v_F(\beta - 1)]$. Expanding the right-hand side of Eq. (8) around q_c, we find the dispersion of the novel gapless plasmon mode ($\omega_{\rm npl}$) to be

$$\omega_{\rm npl}^2 \approx \frac{8n_2 e^2}{\epsilon_0\epsilon_r}\frac{\hbar v_F^3(1+\beta)^2}{\mu^2\beta}(q - q_c), \quad \text{for } \mathbf{q} = q\hat{z}. \quad (10)$$

More remarkably, this low-energy finite-q plasmon mode lies in the PHC gap arising from the open nature of the Fermi surface along the q_z direction. Consequently, this novel mode remains undamped (for $q_c < q_{eh}$; see Sec. S11 in the Supplemental Material [27]) with a large quality factor until it enters the PHC [see Fig. 1(d)]. Physically, this novel mode arises from the out-of-phase *intranode* density oscillations of the electron and hole fluids in a type-II DSM [31].

Note that we have adopted the hydrodynamic theory, which works well only in the long-wavelength ($q \to 0$) limit, in order to find the finite-$q > q_c$ collective mode. Thus, the q_c derived here will be quantitatively different from the exact q_c calculated below, although the qualitative behavior is identical. Going beyond the hydrodynamic theory, we now explicitly calculate the interacting density response function. The electron-electron interaction will be treated within the random phase approximation (RPA).

The noninteracting density response (or Lindhard) function of a single Dirac node is given by [21,29,30,32–34]

$$\Pi_\chi^{\rm NI}(\mathbf{q},\omega) = \frac{g_s}{V}\sum_{\mathbf{k},\lambda,\lambda'}\frac{f(\varepsilon_{\lambda\mathbf{k}}^\chi) - f(\varepsilon_{\lambda'\mathbf{k}+\mathbf{q}}^\chi)}{\hbar\omega^+ + \varepsilon_{\lambda\mathbf{k}}^\chi - \varepsilon_{\lambda'\mathbf{k}+\mathbf{q}}^\chi}F_{\lambda\lambda'}(\mathbf{k},\mathbf{q}). \quad (11)$$

Here, V is the volume, $\omega^+ = \omega + i\eta$ with $\eta \to 0$, and $F_{\lambda\lambda'}(\mathbf{k},\mathbf{q})$ is the orbital overlap function. The Fermi function $f(\varepsilon)$ acts as a step function at $T = 0$. The total density response function includes both nodes: $\Pi^{\rm NI} = \Pi_+^{\rm NI} + \Pi_-^{\rm NI}$. The analytical calculation of $\Pi^{\rm NI}$ for both type-I and type-II DSM is detailed in Secs. S3 and S4 of the Supplemental Material [27]. The density response function for an interacting electron fluid, within RPA, is given by

$$\Pi^{\rm RPA}(\mathbf{q},\omega) = \Pi^{\rm NI}(\mathbf{q},\omega)/\epsilon(\mathbf{q},\omega). \quad (12)$$

Here, $\epsilon(\mathbf{q},\omega) \equiv 1 - V_q\Pi^{\rm NI}(\mathbf{q},\omega)$ is the dynamical dielectric function. The plasmon dispersion and damping constant $\omega_{\rm pl}(\mathbf{q}) - i\gamma_{\rm pl}(\mathbf{q})$ can now be obtained from the poles of $\Pi^{\rm RPA}(\mathbf{q},\omega)$ or, alternately, from the complex roots of $\epsilon(\mathbf{q},\omega) = 0$. For small damping rate, an expansion of

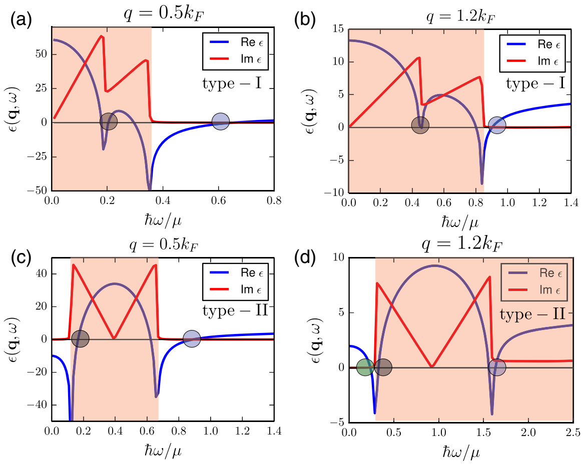

FIG. 2. The real and imaginary parts of the dielectric function $\epsilon(\mathbf{q},\omega)$ for two different values of q along the tilt axis, for (a),(b) type-I and (c),(d) type-II DSM. The shaded region depicts the PHC, and the circles denote the zeros of $\epsilon(\mathbf{q},\omega)$ corresponding to collective excitations. The blue circle is the regular gapped plasmon, while the gray circle is the highly damped mode arising from the out-of-phase oscillation of the electron fluids in different nodes. The green circle in (d) is the novel gapless plasmon mode arising from the out-of-phase oscillations of the intranode electron-hole pockets in a type-II DSM. Other parameters are identical to those of Fig. 1.

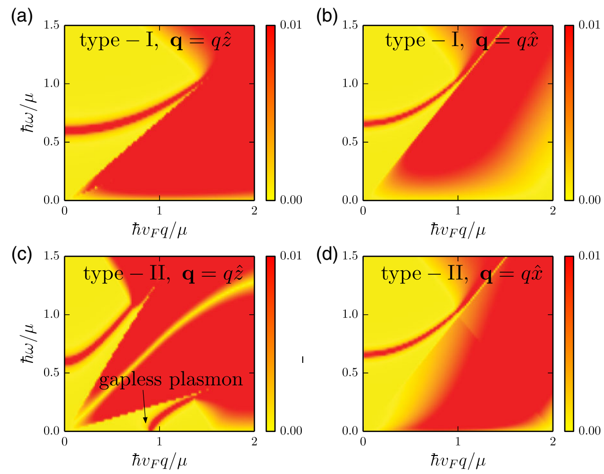

FIG. 3. The RPA loss function $\mathcal{E}_{\rm loss}(\mathbf{q},\omega)$ for (a),(b) type-I and (c),(d) type-II DSM along different directions. The anisotropic band structure results in an anisotropic plasmon gap. The PHC gap in the low-energy finite-q loss function and the existence of the novel undamped plasmon mode for $\mathbf{q}$ along the tilt axis is evident in (c). Other parameters are identical to those of Fig. 1.

$\epsilon(\mathbf{q},\omega)$ around $\omega_{\rm pl}$ yields $\gamma_{\rm pl} = [{\rm Im}(\epsilon)/\partial_\omega {\rm Re}(\epsilon)]|_{\omega_{\rm pl}} > 0$. For a stable plasmon mode $\gamma_{\rm pl} > 0$.

The dielectric function for both type-I and type-II DSM is shown in Fig. 2 for $\mathbf{q}(= q\hat{z})$ along the tilt axis. Figures 2(a) and 2(b) for a type-I DSM show the existence of two stable plasmon modes (same sign of ${\rm Im}[\epsilon]$ and $\partial_\omega{\rm Re}[\epsilon]$, at the ${\rm Re}[\epsilon] = 0$ crossings). The rightmost root of ${\rm Re}[\epsilon] = 0$ with a vanishingly small ${\rm Im}[\epsilon]$ is the gapped 3D Dirac plasmon mode [9,35]. The other root of ${\rm Re}[\epsilon] = 0$ is the damped plasmon mode. It lies in the PHC and corresponds to the out-of-phase oscillations of the electron fluids in different Dirac nodes (see Fig. S2 in the Supplemental Material [27]). The dielectric function for a type-II DSM is shown in Figs. 2(c) and 2(d) for small and large q along the tilt axis, respectively. For small q in Fig. 2(c), there are two stable collective modes: the 3D gapped Dirac plasmon and the Landau damped mode, originating from the out-of-phase *internode* density oscillations. This changes drastically for large q_z in Fig. 2(d), with the emergence of the novel undamped gapless plasmon mode for $q_z > q_c$ at low energies, as predicted by the hydrodynamic theory. Physically, this mode corresponds to out-of-phase intranode density oscillations in the electron and hole pockets in type-II DSM [31].

Experimentally, plasmon resonances also appear as peaks in the momentum-resolved electron energy loss spectrum (EELS), which probes the loss function $\mathcal{E}_{\rm loss}(\mathbf{q},\omega) = -{\rm Im}[1/\epsilon(\mathbf{q},\omega)]$. The loss function for the type-I and type-II DSMs, for $\mathbf{q}$ along different directions, is shown in Fig. 3. For type-I DSM, the gapped Dirac plasmon mode with an anisotropic energy gap is evident in Figs. 3(a) and 3(b), for $\mathbf{q} = q\hat{z}$ and $\mathbf{q} = q\hat{x}$, respectively. The Landau damped, out-of-phase internode plasmon mode lies within the PHC spectrum in Fig. 3(a), and it is not clearly visible.

The RPA loss function $\mathcal{E}_{\rm loss}(\mathbf{q},\omega)$ for a type-II DSM is shown in Figs. 3(c) and 3(d), for $\mathbf{q} = q\hat{z}$ and $\mathbf{q} = q\hat{x}$, respectively. Figure 3(c) clearly highlights the (i) PHC gap in the low-energy but finite-q loss spectrum for q along the tilt axis, and (ii) the existence of the novel undamped gapless plasmon mode (for $q > q_c$) [36]. Our analytical calculations for the density response function coupled with the RPA yield the critical wave vector (for $\beta > 1$) to be

$$q_c \approx \frac{\mu}{\hbar v_F}\sqrt{\frac{2 g_s \alpha_{\rm fine}}{\pi} G(\beta)}, \quad \text{where } G(\beta) = \beta \ln\frac{\beta+1}{\beta-1} - 2, \tag{13}$$

and $\alpha_{\rm fine} = e^2/(4\pi\epsilon_0\epsilon_r\hbar v_F)$ is the effective fine structure constant. For $q > q_c$ and for low energies, the novel gapless plasmon mode disperses as

$$\omega_{\rm npl}^2 \approx v_F^2(\beta^2 - 1)^2 G(\beta) q_c (q - q_c). \tag{14}$$

The $\omega_{\rm npl} \propto (q - q_c)^{1/2}$ behavior is qualitatively consistent with the results from the hydrodynamic theory, albeit with a different prefactor. The normal gapped plasmon mode in both type-I and type-II DSM has an anisotropic plasmon gap, owing to the anisotropic electronic dispersion. In a type-II DSM, the plasmon gap $\omega_{\rm pl}(q = 0)$ along the tilt axis is given by the root of the following transcendental equation:

$$\omega^2 = \frac{\mu^2}{\hbar^2}\frac{4g_s\alpha_{\rm fine}}{3\pi\gamma(\omega)}, \qquad \gamma(\omega) = 1 + \frac{g_s\alpha_{\rm fine}}{3\pi}\ln\left|\frac{4\mathcal{E}_{\rm max}^2}{4\mu^2-\omega^2}\right|. \tag{15}$$

Here, the plasmon gap scales as $\omega_{\rm pl}(q=0) \propto \mu \propto n$, in contrast to the $\omega_{\rm pl} \propto n^{2/3}$ scaling in type-I DSM.

The normal gapped plasmon mode was recently observed in $PtTe_2$ (a type-II DSM) along the direction perpendicular to the tilt axis (along Γ–K) by means of high-resolution EELS (HREELS) [9,20]. HREELS analyzes the electrons reflected by the crystal surface with an energy resolution of a few meV [9,20] and can transfer only momentum components parallel to the cleavage surface ($q_\parallel$) [37]. Therefore, plasmons along the tilt axis (Γ–A) are generally inaccessible to HREELS and also to other scattering techniques used to study the dispersion relation of low-energy collective modes, such as inelastic helium atom scattering [38]. Conversely, momentum-resolved EELS with transmission electron microscopy (EELS-TEM) easily enables probing excitations along Γ–A. Unfortunately, the energy resolution of most EELS-TEM apparatuses (>200 meV [39]) is largely inadequate to detect gapless excitations. Nevertheless, recent technological advancements have been decisive in improving the energy resolution up to 18–50 meV [40,41], with the next target to reach 5 meV [42]. Consequently, it is expected that in a few years the measurement of the dispersion relation of plasmonic modes along the tilt axis (Γ–A) will be experimentally feasible.

In summary, we predict a novel undamped gapless plasmon mode in a type-II DSM, arising from the presence of both electron and hole pockets at the Fermi energy. This novel mode exists beyond a critical wave vector and only along the direction of the tilt axis. Physically, it arises due to the out-of-phase oscillation of the density deviations in the electron and the hole pockets. Such a gapless mode can also arise in other nontopological semimetals with open Fermi surfaces, though its undamped nature has to be explored carefully. A similar gapless (and possibly undamped) plasmon mode is also expected to arise in type-II WSM.

A. A. and K. S. thank Sougata Mardanya and Barun Ghosh for stimulating discussions. A. A. acknowledges the Science Education and Research Board (SERB) and Department of Science and Technology (DST) of the government of India for financial support.

*amitag@iitk.ac.in

[1] A. Bansil, H. Lin, and T. Das, Colloquium: Topological band theory, Rev. Mod. Phys. **88**, 021004 (2016).

[2] N. P. Armitage, E. J. Mele, and A. Vishwanath, Weyl and Dirac semimetals in three-dimensional solids, Rev. Mod. Phys. **90**, 015001 (2018).

[3] A. A. Burkov, Topological semimetals, Nat. Mater. **15**, 1145 (2016).

[4] B. J. Yang and N. Nagaosa, Classification of stable three-dimensional Dirac semimetals with nontrivial topology, Nat. Commun. **5**, 4898 (2014).

[5] A. A. Soluyanov, D. Gresch, Z. Wang, Q. Wu, M. Troyer, X. Dai, and B. A. Bernevig, Type-II Weyl semimetals, Nature (London) **527**, 495 (2015).

[6] T.-R. Chang, S.-Y. Xu, D. S. Sanchez, W.-F. Tsai, S.-M. Huang, G. Chang, C.-H. Hsu, G. Bian, I. Belopolski, Z.-M. Yu, S. A. Yang, T. Neupert, H.-T. Jeng, H. Lin, and M. Z. Hasan, Type-II Symmetry-Protected Topological Dirac Semimetals, Phys. Rev. Lett. **119**, 026404 (2017).

[7] Z. Song and X. Dai, Hear the Sound of Weyl Fermions, Phys. Rev. X **9**, 021053 (2019).

[8] M. Yan, H. Huang, K. Zhang, E. Wang, W. Yao, K. Deng, G. Wan, H. Zhang, M. Arita, H. Yang, Z. Sun, H. Yao, Y. Wu, S. Fan, W. Duan, and S. Zhou, Lorentz-violating type-II Dirac fermions in transition metal dichalcogenide $PtTe_2$, Nat. Commun. **8**, 257 (2017).

[9] A. Politano, G. Chiarello, B. Ghosh, K. Sadhukhan, C.-N. Kuo, C. Shan Lue, V. Pellegrini, and A. Agarwal, 3D Dirac Plasmons in the Type-II Dirac Semimetal $PtTe_2$, Phys. Rev. Lett. **121**, 086804 (2018).

[10] Z. Wang, Y. Sun, X. Q. Chen, C. Franchini, G. Xu, H. Weng, X. Dai, and Z. Fang, Dirac semimetal and topological phase transitions in A3Bi (A = Na, K, Rb), Phys. Rev. B **85**, 195320 (2012).

[11] Z. K. Liu, B. Zhou, Y. Zhang, Z. J. Wang, H. M. Weng, D. Prabhakaran, S. Mo, Z. X. Shen, Z. Fang, X. Dai, Z. Hussain, and Y. L. Chen, Topological Dirac semimetal, Na3Bi, Science **343**, 864 (2014).

[12] Z. Wang, H. Weng, Q. Wu, X. Dai, and Z. Fang, Three-dimensional Dirac semimetal and quantum transport in Cd_3As_2, Phys. Rev. B **88**, 125427 (2013).

[13] Z. K. Liu, J. Jiang, B. Zhou, Z. J. Wang, Y. Zhang, H. M. Weng, D. Prabhakaran, S. K. Mo, H. Peng, P. Dudin, T. Kim, M. Hoesch, Z. Fang, X. Dai, Z. X. Shen, D. L. Feng, Z. Hussain, and Y. L. Chen, A stable three-dimensional topological Dirac semimetal Cd_3As_2, Nat. Mater. **13**, 677 (2014).

[14] M. S. Bahramy *et al.*, Ubiquitous formation of bulk Dirac cones and topological surface states from a single orbital manifold in transition-metal dichalcogenides, Nat. Mater. **17**, 21 (2018).

[15] K. Zhang, M. Yan, H. Zhang, H. Huang, M. Arita, Z. Sun, W. Duan, Y. Wu, and S. Zhou, Experimental evidence for type-II Dirac semimetal in $PtSe_2$, Phys. Rev. B **96**, 125102 (2017).

[16] H.-J. Noh, J. Jeong, E.-J. Cho, K. Kim, B. I. Min, and B.-G. Park, Experimental Realization of Type-II Dirac Fermions in a $PdTe_2$ Superconductor, Phys. Rev. Lett. **119**, 016401 (2017).

[17] F. Fei, X. Bo, R. Wang, B. Wu, J. Jiang, D. Fu, M. Gao, H. Zheng, Y. Chen, X. Wang, H. Bu, F. Song, X. Wan, B. Wang, and G. Wang, Nontrivial berry phase and type-II Dirac transport in the layered material $PdTe_2$, Phys. Rev. B **96**, 041201(R) (2017).

[18] K. Das and A. Agarwal, Linear magnetochiral transport in tilted type-I and type-II Weyl semimetals, Phys. Rev. B **99**, 085405 (2019).

[19] S. Nandy, G. Sharma, A. Taraphder, and S. Tewari, Chiral Anomaly as the Origin of the Planar Hall Effect in Weyl Semimetals, Phys. Rev. Lett. **119**, 176804 (2017).

[20] B. Ghosh, F. Alessandro, M. Zappia, R. Brescia, C.-N. Kuo, C. S. Lue, G. Chiarello, A. Politano, L. S. Caputi, A. Agarwal, and A. Cupolillo, Broadband excitation spectrum of bulk crystals and thin layers of $PtTe_2$, Phys. Rev. B **99**, 045414 (2019).

[21] R. Sachdeva, A. Thakur, G. Vignale, and A. Agarwal, Plasmon modes of a massive Dirac plasma, and their superlattices, Phys. Rev. B **91**, 205426 (2015).

[22] S. Das Sarma and A. Madhukar, Collective modes of spatially separated, two-component, two-dimensional plasma in solids, Phys. Rev. B **23**, 805 (1981).

[23] R. Sensarma, E. H. Hwang, and S. Das Sarma, Dynamic screening and low-energy collective modes in bilayer graphene, Phys. Rev. B **82**, 195428 (2010).

[24] A. Agarwal, M. Polini, G. Vignale, and M. E. Flatté, Long-lived spin plasmons in a spin-polarized two-dimensional electron gas, Phys. Rev. B **90**, 155409 (2014).

[25] B. Singh, S. Mardanya, C. Su, H. Lin, A. Agarwal, and A. Bansil, Spin-orbit coupling driven crossover from a starfruitlike nodal semimetal to Dirac and Weyl semimetal state in CaAuAs, Phys. Rev. B **98**, 085122 (2018).

[26] H. Huang, S. Zhou, and W. Duan, Type-II Dirac fermions in the $PtSe_2$ class of transition metal dichalcogenides, Phys. Rev. B **94**, 121117(R) (2016).

[27] See Supplemental Material at http://link.aps.org/supplemental/10.1103/PhysRevLett.124.046803, which includes (i) details of the Fermi surface and calculation and PHC, (ii) analytical results for the noninteracting density-density response function, (iii) the gapped plasmon mode in type-I and type-II DSM, and (iv) the dispersion of the gapless plasmon mode in type-II DSM.

[28] A. Thakur, R. Sachdeva, and A. Agarwal, Dynamical polarizability, screening and plasmons in one, two and three dimensional massive Dirac systems, J. Phys. Condens. Matter **29**, 105701 (2017).

[29] A. Thakur, K. Sadhukhan, and A. Agarwal, Dynamic current-current susceptibility in three-dimensional Dirac and Weyl semimetals, Phys. Rev. B **97**, 1 (2018).

[30] G. F. Giuliani and G. Vignale, *Quantum Theory of the Electron Liquid* (Cambridge University Press, Cambridge, England, 2005).

[31] This can be shown explicitly in the $q \to 0$ limit, using the matrix form of the coupled hydrodynamic equations for the electron and hole density deviations.

[32] A. Agarwal, S. Chesi, T. Jungwirth, J. Sinova, G. Vignale, and M. Polini, Plasmon mass and Drude weight in strongly spin-orbit-coupled two-dimensional electron gases, Phys. Rev. B **83**, 115135 (2011).

[33] B. Ghosh, P. Kumar, A. Thakur, Y. S. Chauhan, S. Bhowmick, and A. Agarwal, Anisotropic plasmons, excitons, and electron energy loss spectroscopy of phosphorene, Phys. Rev. B **96**, 035422 (2017).

[34] K. Sadhukhan and A. Agarwal, Anisotropic plasmons, Friedel oscillations, and screening in $8-Pmmn$ borophene, Phys. Rev. B **96**, 035410 (2017).

[35] G. Chiarello, J. Hofmann, Z. Li, V. Fabio, L. Guo, X. Chen, S. Das Sarma, and A. Politano, Tunable surface plasmons in Weyl semimetals TaAs and NbAs, Phys. Rev. B **99**, 121401(R) (2019).

[36] In some type-II Dirac semimetals, in addition to the open Fermi surfaces, there can be additional closed Fermi pockets, which may have PHC spectrum for low energies and finite q. These Fermi pockets can lead to some Landau damping and quench the plasmon intensity of the novel plasmon mode. We have numerically checked that the novel plasmon mode survives such Landau damping and is still long-lived with a prominent peak in the energy loss spectrum (see Sec. S12 in the Supplemental Material [27]).

[37] H. Ibach and D. L. Mills, *Electron Energy Loss Spectroscopy and Surface Vibrations* (Academic Press, New York, 1982).

[38] G. Benedek, J. Ellis, A. Reichmuth, P. Ruggerone, H. Schief, and J. P. Toennies, Organ-Pipe Modes of Sodium Epitaxial Multilayers on Cu(001) Observed by Inelastic Helium-Atom Scattering, Phys. Rev. Lett. **69**, 2951 (1992).

[39] R. F. Egerton, Electron energy-loss spectroscopy in the TEM, Rep. Prog. Phys. **72**, 016502 (2009).

[40] F. S. Hage, R. J. Nicholls, J. R. Yates, D. G. McCulloch, T. C. Lovejoy, N. Dellby, O. L. Krivanek, K. Refson, and Q. M. Ramasse, Nanoscale momentum-resolved vibrational spectroscopy, Sci. Adv. **4**, eaar7495 (2018).

[41] A. A. Govyadinov, A. Konečná, A. Chuvilin, S. Vélez, I. Dolado, A. Y. Nikitin, S. Lopatin, F. Casanova, L. E. Hueso, J. Aizpurua, and R. Hillenbrand, Probing low-energy hyperbolic polaritons in van der Waals crystals with an electron microscope, Nat. Commun. **8**, 95 (2017).

[42] T. C. Lovejoy, N. J. Bacon, A. L. Bleloch, N. Dellby, M. V. Hoffman, and O. L. Krivanek, Ultra-high energy resolution eels, Microsc. Microanal. **23**, 1552 (2017).